

Deterministic Inversion of Wideband GPR Data for Multi-Resolution Imaging of Buried Objects

M. Salucci, L. Poli, and A. Massa

Abstract

In this work, the performance of an innovative conjugate-gradient (*CG*)-based deterministic microwave imaging technique are assessed for the inversion of wideband ground penetrating radar (*GPR*) data. The developed methodology exploits the intrinsic frequency diversity of *GPR* measurements through a multi-frequency (*MF*) strategy in order to add information to the inversion problem and to mitigate the negative effects of ill-posedness of the buried inverse scattering (*IS*) problem. Moreover, the iterative multi-scaling approach (*IMSA*) is exploited in order to increase as much as possible the ratio between non-redundant data and problem unknowns, thus mitigating the problem of the non-linearity. Some numerical results are shown, in order to analyze the achievable reconstruction capabilities by the developed *MF* technique when dealing with the retrieval of objects having different values of relative permittivity. A direct comparison with a frequency hopping (*FH*)-based implementation of the same multi-resolution deterministic solver is shown, as well, to highlight the differences between the two approaches.

1 Definitions

1.1 Glossary

- D_{inv} : investigation domain;
- D_{obs} : observation domain;
- N : number of discretization cells in D_{ind} ;
- V : number of views;
- M : number of measurement points;
- F : number of frequencies considered for the inversion;
- (x_v, y_v) : coordinates of the v -th source ($v = 1, \dots, V$).
- (x_m^v, y_m^v) : coordinates of the m -th measurement point for the v -th view v , ($m = 1, \dots, M$);
- $\varepsilon_{ra} = \frac{\varepsilon_a}{\varepsilon_0}$: relative electric permittivity for the upper half-space ($y > 0$);
- σ_a : conductivity for the upper half-space ($y > 0$);
- $\varepsilon_{rb} = \frac{\varepsilon_b}{\varepsilon_0}$: background relative electric permittivity;
- σ_b : background conductivity;

2 Variation of the Object Permittivity

2.1 Circular object ($\sigma_{obj} = 10^{-3}$ [S/m])

2.1.1 Parameters

Background

Inhomogeneous and nonmagnetic background composed by two half spaces

- Upper half space ($y > 0$ - air): $\varepsilon_{ra} = 1.0$, $\sigma_a = 0.0$;
- Lower half space ($y < 0$ - soil): $\varepsilon_{rb} = 4.0$, $\sigma_b = 10^{-3}$ [S/m];

Investigation domain (D_{inv})

- Side: $L_{D_{inv}} = 0.8$ [m];
- Barycenter: $(x_{bar}^{D_{inv}}, y_{bar}^{D_{inv}}) = (0.00, -0.4)$ [m];

Time-Domain forward solver ($FDTD - GPRMax2D$)

- Side of the simulated domain: $L = 6$ [m];
- Number of cells: $N^{FDTD} = 750 \times 750 = 5.625 \times 10^5$;
- Side of the $FDTD$ cells $l^{FDTD} = 0.008$ [m];
- Simulation time window: $T^{FDTD} = 20 \times 10^{-9}$ [sec];
- Time step: $\Delta t^{FDTD} = 1.89 \times 10^{-11}$ [sec];
- Number of time samples: $N_t^{FDTD} = 1060$;
- Boundary conditions: perfectly matched layer (PML);
- Source type: Gaussian mono-cycle (first Gaussian pulse derivative, called "Ricker" in $GPRMax2D$)
 - Central frequency: $f_0 = 300$ [MHz];
 - Source amplitude: $A = 1.0$ [A];

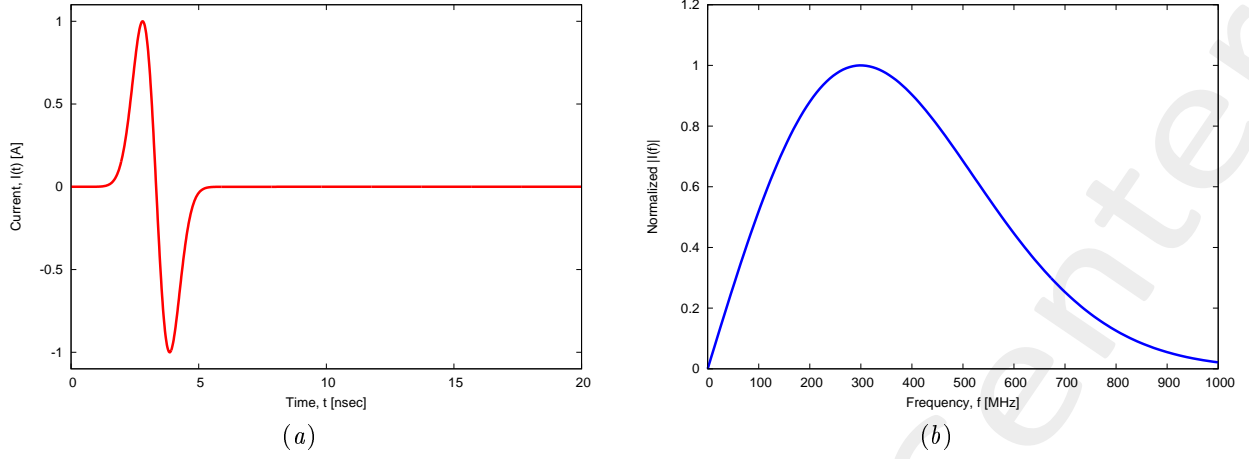


Figure 1: *GPRMax2D* excitation signal. (a) Time pulse, (b) normalized frequency spectrum.

Frequency parameters

- Frequency range: $f \in [f_{min}, f_{max}] = [200.0, 600.0]$ [MHz] [?] (-3 [dB] bandwidth of the Gaussian Monocycle excitation centered at $f_0 = 300$ [MHz]);
- Frequency step: $\Delta f = 100$ [MHz] ($F = 5$ frequency steps in $[f_{min}, f_{max}]$);

| f [MHz] | λ_a [m] | λ_b [m] | f^* [MHz] |
|-----------|-----------------|-----------------|-------------|
| 200.0 | 1.50 | 0.75 | 200.5 |
| 300.0 | 1.00 | 0.50 | 297.6 |
| 400.0 | 0.75 | 0.37 | 401.1 |
| 500.0 | 0.60 | 0.30 | 498.1 |
| 600.0 | 0.50 | 0.25 | 601.6 |

Table 1: Considered frequencies and corresponding wavelength in the upper medium (λ_a , free space) and in the lower medium (λ_b , soil). f^* is the nearest frequency sample available from transformed time-domain data, and represents the real frequency considered by the inversion algorithm.

Scatterer

- Type: Circular;
- Barycenter: $(x_{obj}, y_{obj}) = (-0.16, -0.4)$ [m];
- Radius: $r_{obj} = 0.08$ [m];
- Electromagnetic properties: $\varepsilon_{r,obj} = \{5.0; 5.5; 6.5\}$, $\sigma_{obj} = 10^{-3}$ [S/m] ($\sigma_{obj} = \sigma_b$);
- Contrast function: $\tau = \{1.0; 1.5; 2.5\}$

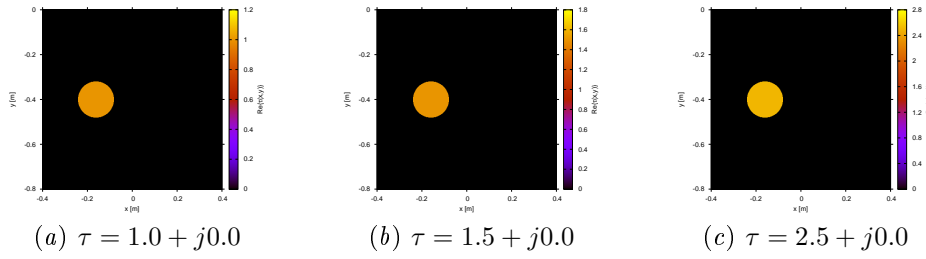


Figure 2: Actual object.

Measurement setup

- Considered frequency: $f_{min} = 200$ [MHz], $\lambda_b = 0.75$ [m].
- #DoFs = $2ka = \frac{2\pi}{\lambda_b} L\sqrt{2} = \frac{2\pi}{0.75} 0.8\sqrt{2} \simeq 9.5$;
- Number of views (sources): $V = 10$;
 - $\min\{x_v\} = -0.5$ [m], $\max\{x_v\} = 0.5$ [m];
 - height: $y_v = 0.1$ [m], $\forall v = 1, \dots, V$;
- Number of measurement points: $M = 9$;
 - $\min\{x_m\} = -0.5$ [m], $\max\{x_m\} = 0.5$ [m];
 - height: $y_m = 0.1$ [m], $\forall m = 1, \dots, M$;

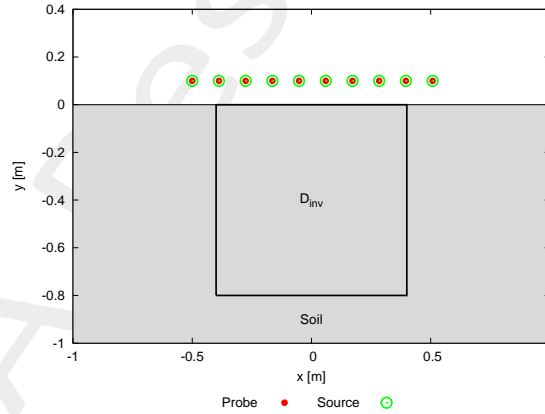


Figure 3: Location of the measurement points ($M = 9$) and of the sources ($V = 10$). Only one source is active for each view.

Inverse solver parameters

- Shared parameters
 - Weight of the state term of the functional: 1.0;
 - Weight of the data term of the functional: 1.0;
 - Convergence threshold: 10^{-10} ;

- Variable ranges:
 - * $\sigma \in [8.0 \times 10^{-4}, 1.2 \times 10^{-3}]$ [S/m];
 - * $\Re \{E_{tot}^{int}\} \in [-8, 8]$, $\Im \{E_{tot}^{int}\} \in [-8, 8]$;
- Degrees of freedom:
 - * Considered frequency: $f_{min} = 200$ [MHz], $\lambda_b = 0.75$ [m];
 - * $\frac{(2ka)^2}{2} = \frac{(2 \times \frac{2\pi}{\lambda_b} \times \frac{L\sqrt{2}}{2})^2}{2} = 4\pi^2 \left(\frac{L}{\lambda_b}\right)^2 = 4\pi^2 \left(\frac{0.8}{0.75}\right)^2 \simeq 44.87$;
- Number of cells: $N = 49 = 7 \times 7$;
- Maximum number of *IMSA* steps: $S = 4$;
- Side ratio threshold: $\eta_{th} = 0.2$;

- ***MF – IMSA – CG* parameters**

- Maximum number of iterations: $I = 200$;

- ***FH – IMSA – CG* parameters**

- Maximum number of iterations: $I = 400$;

Signal to noise ratio (on $E_{tot}(t)$)

- $SNR = \{50, 40, 30, 20\}$ [dB] + Noiseless data.

2.1.2 $\varepsilon_{r,obj} = 5.0$ ($\tau = 1.0$): Final reconstructions ($@f_{max} = 600$ [MHz])

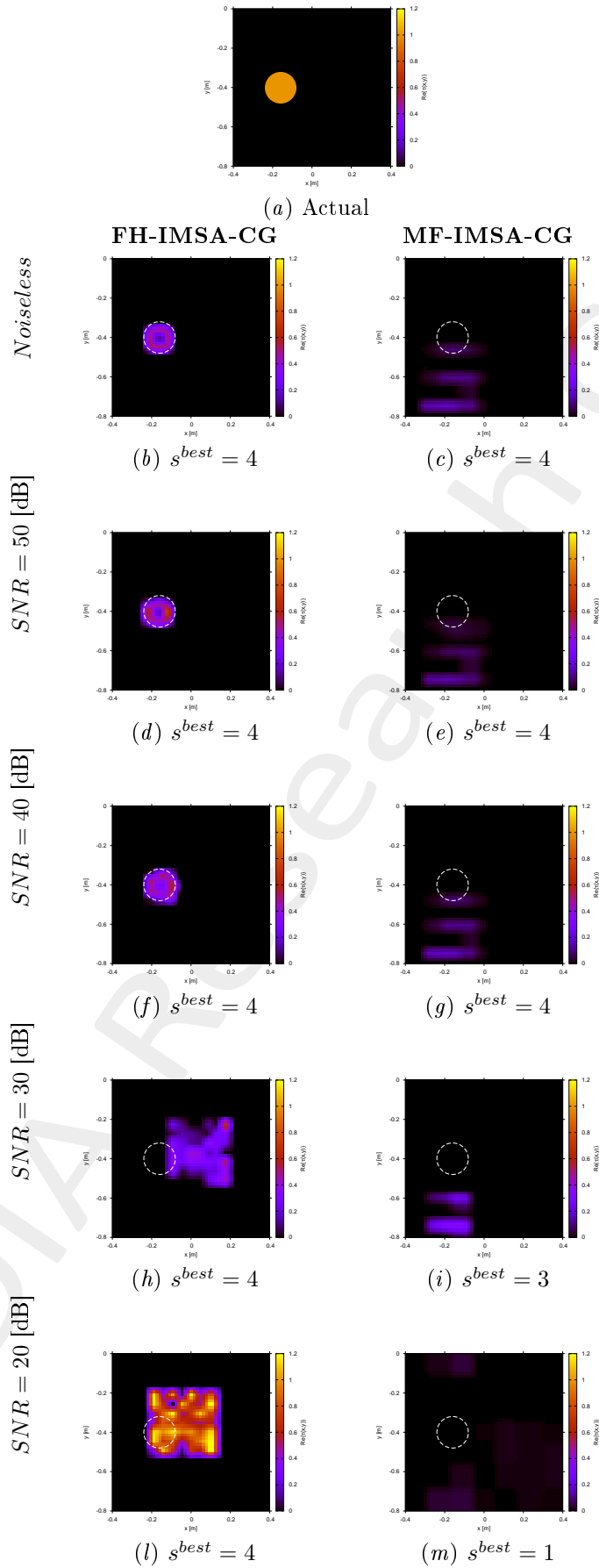


Figure 4: *FH-IMSA-CG* vs. *MF-IMSA-CG*: Retrieved dielectric profiles at the *IMSA* convergence step (s^{best}).

2.1.3 $\varepsilon_{r,obj} = 5.5$ ($\tau = 1.5$): Final reconstructions ($@f_{max} = 600$ [MHz])

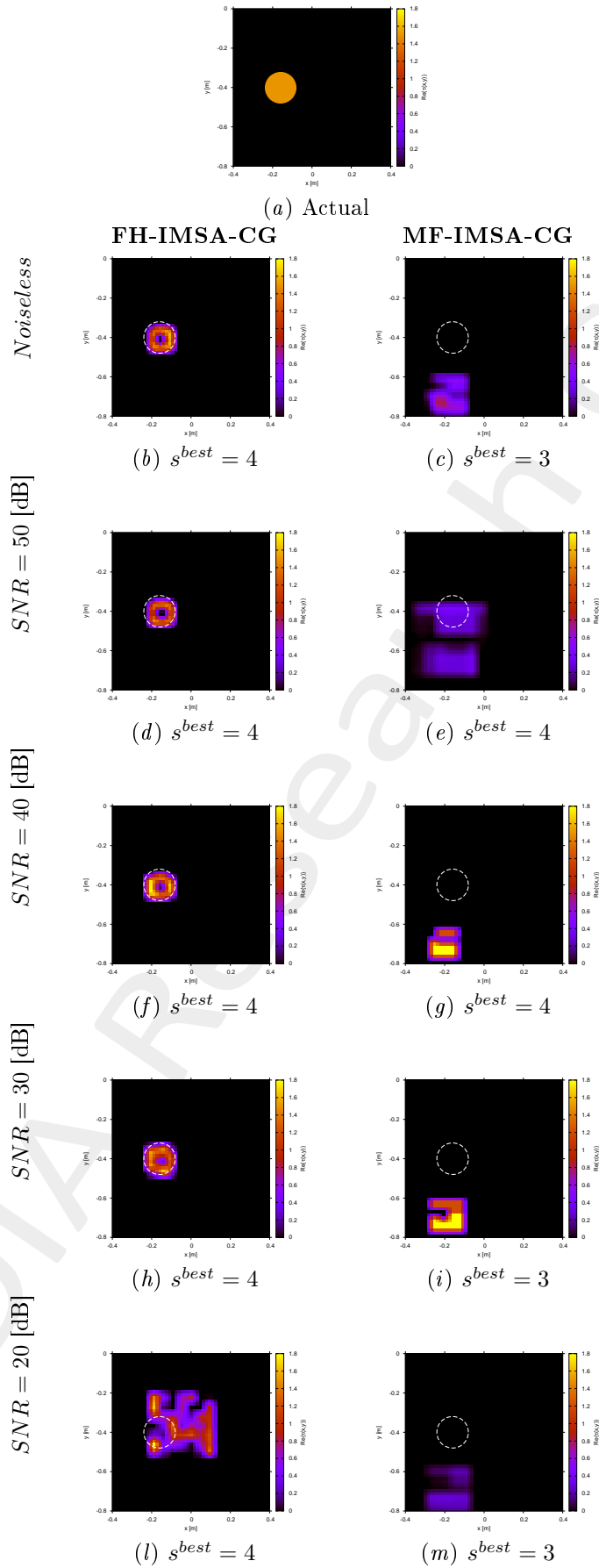


Figure 5: *FH-IMSA-CG* vs. *MF-IMSA-CG*: Retrieved dielectric profiles at the *IMSA* convergence step (s^{best}).

2.1.4 $\varepsilon_{r,obj} = 6.5$ ($\tau = 2.5$): Final reconstructions ($@f_{max} = 600$ [MHz])

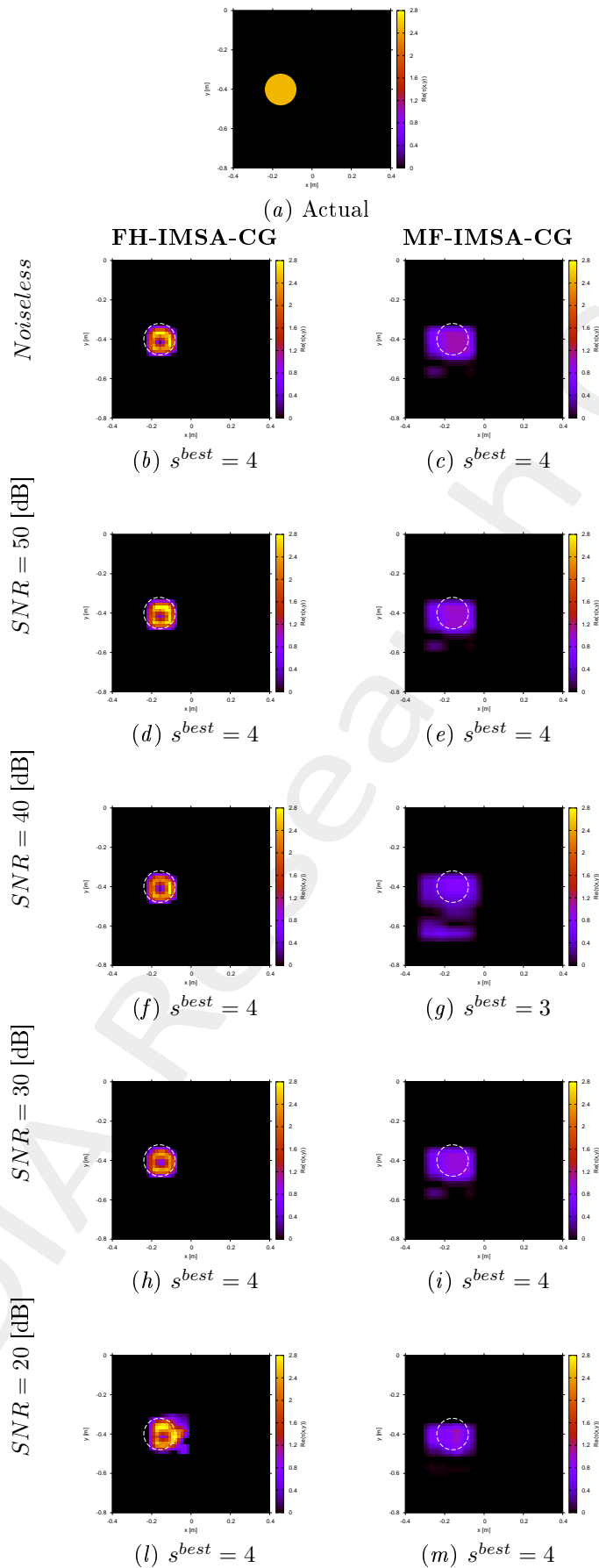


Figure 6: *FH-IMSA-CG* vs. *MF-IMSA-CG*: Retrieved dielectric profiles at the *IMSA* convergence step (s^{best}).

References

- [1] P. Rocca, M. Benedetti, M. Donelli, D. Franceschini, and A. Massa, "Evolutionary optimization as applied to inverse problems," *Inverse Probl.*, vol. 25, pp. 1-41, Dec. 2009.
- [2] P. Rocca, G. Oliveri, and A. Massa, "Differential Evolution as applied to electromagnetics," *IEEE Antennas Propag. Mag.*, vol. 53, no. 1, pp. 38-49, Feb. 2011.
- [3] M. Salucci, G. Oliveri, and A. Massa, "GPR prospecting through an inverse scattering frequency-hopping multi-focusing approach," *IEEE Trans. Geosci. Remote Sens.*, vol. 53, no. 12, pp. 6573-6592, Dec. 2015.
- [4] M. Salucci, L. Poli, N. Anselmi and A. Massa, "Multifrequency particle swarm optimization for enhanced multiresolution GPR microwave imaging," *IEEE Trans. Geosci. Remote Sens.*, vol. 55, no. 3, pp. 1305-1317, Mar. 2017.
- [5] A. Massa, P. Rocca, and G. Oliveri, "Compressive sensing in electromagnetics - A review," *IEEE Antennas Propag. Mag.*, pp. 224-238, vol. 57, no. 1, Feb. 2015.
- [6] A. Massa and F. Teixeira, Guest-Editorial: Special Cluster on Compressive Sensing as Applied to Electromagnetics, *IEEE Antennas Wireless Propag. Lett.*, vol. 14, pp. 1022-1026, 2015.
- [7] N. Anselmi, G. Oliveri, M. Salucci, and A. Massa, "Wavelet-based compressive imaging of sparse targets," *IEEE Trans. Antennas Propag.*, vol. 63, no. 11, pp. 4889-4900, Nov. 2015.
- [8] G. Oliveri, N. Anselmi, and A. Massa, "Compressive sensing imaging of non-sparse 2D scatterers by a total-variation approach within the Born approximation," *IEEE Trans. Antennas Propag.*, vol. 62, no. 10, pp. 5157-5170, Oct. 2014.
- [9] T. Moriyama, G. Oliveri, M. Salucci, and T. Takenaka, "A multi-scaling forward-backward time-stepping method for microwave imaging," *IEICE Electron. Expr.*, vol. 11, no. 16, pp. 1-12, Aug. 2014.
- [10] T. Moriyama, M. Salucci, M. Tanaka, and T. Takenaka, "Image reconstruction from total electric field data with no information on the incident field," *J. Electromagnet. Wave.*, vol. 30, no. 9, pp. 1162-1170, 2016.
- [11] F. Viani, L. Poli, G. Oliveri, F. Robol, and A. Massa, "Sparse scatterers imaging through approximated multi-task compressive sensing strategies," *Microw. Opt. Technol. Lett.*, vol. 55, no. 7, pp. 1553-1557, Jul. 2013.
- [12] M. Salucci, L. Poli, and A. Massa, "Advanced multi-frequency GPR data processing for non-linear deterministic imaging," *Signal Processing - Special Issue on 'Advanced Ground-Penetrating Radar Signal-Processing Techniques'*, vol. 132, pp. 306-318, Mar. 2017.
- [13] M. Salucci, N. Anselmi, G. Oliveri, P. Calmon, R. Miorelli, C. Reboud, and A. Massa, "Real-time NDT-NDE through an innovative adaptive partial least squares SVR inversion approach," *IEEE Trans. Geosci. Remote Sens.*, vol. 54, no. 11, pp. 6818-6832, Nov. 2016.

- [14] L. Poli, G. Oliveri, and A. Massa, "Imaging sparse metallic cylinders through a local shape function bayesian compressing sensing approach," *J. Opt. Soc. Am. A*, vol. 30, no. 6, pp. 1261-1272, Jun. 2013.

ELEDIA Research Center